

**Elastic-Plastic Behavior of Cyclotrimethylene Trinitramine
Single Crystals Under Spherical Indentation:
Modeling and Simulation**

by J. D. Clayton and R. Becker

ARL-RP-364

April 2012

A reprint from the *Journal of Applied Physics*, Vol. 111, pp. 063512-1 to 063512-9, 2012.

NOTICES

Disclaimers

The findings in this report are not to be construed as an official Department of the Army position unless so designated by other authorized documents.

Citation of manufacturer's or trade names does not constitute an official endorsement or approval of the use thereof.

Destroy this report when it is no longer needed. Do not return it to the originator.

Army Research Laboratory

Aberdeen Proving Ground, MD 21005-5066

ARL-RP-364**April 2012**

Elastic-Plastic Behavior of Cyclotrimethylene Trinitramine Single Crystals Under Spherical Indentation: Modeling and Simulation

J. D. Clayton and R. Becker
Weapons and Materials Research Directorate, ARL

A reprint from the *Journal of Applied Physics*, Vol. 111, pp. 063512-1 to 063512-9, 2012.

REPORT DOCUMENTATION PAGE				Form Approved OMB No. 0704-0188	
<p>Public reporting burden for this collection of information is estimated to average 1 hour per response, including the time for reviewing instructions, searching existing data sources, gathering and maintaining the data needed, and completing and reviewing the collection information. Send comments regarding this burden estimate or any other aspect of this collection of information, including suggestions for reducing the burden, to Department of Defense, Washington Headquarters Services, Directorate for Information Operations and Reports (0704-0188), 1215 Jefferson Davis Highway, Suite 1204, Arlington, VA 22202-4302. Respondents should be aware that notwithstanding any other provision of law, no person shall be subject to any penalty for failing to comply with a collection of information if it does not display a currently valid OMB control number.</p> <p>PLEASE DO NOT RETURN YOUR FORM TO THE ABOVE ADDRESS.</p>					
1. REPORT DATE (DD-MM-YYYY)		2. REPORT TYPE		3. DATES COVERED (From - To)	
April 2012		Reprint		October 2010–February 2012	
4. TITLE AND SUBTITLE Elastic-Plastic Behavior of Cyclotrimethylene Trinitramine Single Crystals Under Spherical Indentation: Modeling and Simulation				5a. CONTRACT NUMBER	
				5b. GRANT NUMBER	
				5c. PROGRAM ELEMENT NUMBER	
6. AUTHOR(S) J. D. Clayton and R. Becker				5d. PROJECT NUMBER	
				AH80	
				5e. TASK NUMBER	
7. PERFORMING ORGANIZATION NAME(S) AND ADDRESS(ES) U.S. Army Research Laboratory ATTN: RDRL-WMP-C Aberdeen Proving Ground, MD 21005-5066				5f. WORK UNIT NUMBER	
				8. PERFORMING ORGANIZATION REPORT NUMBER	
				ARL-RP-364	
9. SPONSORING/MONITORING AGENCY NAME(S) AND ADDRESS(ES)				10. SPONSOR/MONITOR'S ACRONYM(S)	
				11. SPONSOR/MONITOR'S REPORT NUMBER(S)	
12. DISTRIBUTION/AVAILABILITY STATEMENT Approved for public release; distribution is unlimited.					
13. SUPPLEMENTARY NOTES A reprint from the <i>Journal of Applied Physics</i> , Vol. 111, pp. 063512-1 to 063512-9, 2012.					
14. ABSTRACT A nonlinear anisotropic elastic-plastic model is developed for single crystals of the energetic material cyclotrimethylene trinitramine (RDX). Numerical simulations of spherical indentation on oriented single crystals are performed; predictions are compared with experimental data and observations from the literature. Model predictions for elastic response and initial yield using elastic constants obtained from resonant ultrasound spectroscopy agree with experimental data; predicted forces using constants obtained from Brillouin scattering tend to exceed experimental data. Influences of elastic anisotropy and elastic nonlinearity are significant. Predicted slip system activity is in reasonable agreement with that deduced from experimental surface profiles when a uniform strength of $G/20$ is assigned to all six slip systems, with G an effective elastic shear modulus. Predicted indentation forces in the post-yield regime exceed those observed in experiments, suggesting that surface and possibly subsurface fractures may contribute to a loss of stiffness in experiments at larger indentation depths.					
15. SUBJECT TERMS energetic material, molecular crystal, RDX, elasticity, plasticity, indentation					
16. SECURITY CLASSIFICATION OF:			17. LIMITATION OF ABSTRACT	18. NUMBER OF PAGES	19a. NAME OF RESPONSIBLE PERSON
a. REPORT	b. ABSTRACT	c. THIS PAGE			John D. Clayton
Unclassified	Unclassified	Unclassified	UU	16	19b. TELEPHONE NUMBER (Include area code)
					410-278-6146

Elastic-plastic behavior of cyclotrimethylene trinitramine single crystals under spherical indentation: Modeling and simulation

J. D. Clayton^{a)} and R. Becker*Impact Physics RDRL-WMP-C, U.S. Army Research Laboratory, Aberdeen Proving Ground, Maryland 21005-5066, USA*

(Received 5 January 2012; accepted 13 February 2012; published online 21 March 2012)

A nonlinear anisotropic elastic-plastic model is developed for single crystals of the energetic material cyclotrimethylene trinitramine (RDX). Numerical simulations of spherical indentation on oriented single crystals are performed; predictions are compared with experimental data and observations from the literature. Model predictions for elastic response and initial yield using elastic constants obtained from resonant ultrasound spectroscopy agree with experimental data; predicted forces using constants obtained from Brillouin scattering tend to exceed experimental data. Influences of elastic anisotropy and elastic nonlinearity are significant. Predicted slip system activity is in reasonable agreement with that deduced from experimental surface profiles when a uniform strength of $G/20$ is assigned to all six slip systems, with G an effective elastic shear modulus. Predicted indentation forces in the post-yield regime exceed those observed in experiments, suggesting that surface and possibly subsurface fractures may contribute to a loss of stiffness in experiments at larger indentation depths. [<http://dx.doi.org/10.1063/1.3695392>]

I. INTRODUCTION

Defects in energetic materials are thought to affect their initiation sensitivity. Stresses concentrate in the vicinity of cracks, pores, or lattice defects, which in turn can affect initiation of reactions associated with burning or detonation. In single crystals, availability of slip systems associated with mobile dislocations may lower peak stresses and decrease sensitivity to shock initiation.¹

The focus of the present work is the mechanical behavior of the energetic material cyclotrimethylene trinitramine ($C_3H_6N_6O_6$), referred to as RDX (Research Development eXplosive). Single crystals of RDX belong to an orthorhombic space group with eight molecules per unit cell. Dislocations in RDX have been characterized using etch pit² and x ray topographic^{3,4} techniques. Likely slip systems in RDX have been suggested from analysis of anisotropic hardness profiles⁵ and indentation experiments.^{6,7} The latter experiments^{6,7} also provide an estimate of the critical resolved shear stress associated with slip initiation, thought to be on the order of the theoretical strength (i.e., $\approx G/10$ – $G/20$, with G a representative elastic shear modulus), which corresponds to homogeneous dislocation nucleation. Inelastic behavior of RDX crystals has also been probed using shock experiments^{1,8} and molecular dynamics simulations.^{8,9}

Continuum crystal plasticity theory permits predictive mesoscale modeling of materials' behavior at length scales larger than that feasible using molecular models, but with greater resolution than that afforded by macroscopic elastic-plastic models that omit anisotropy and slip system activity. Grain interactions can be studied in direct numerical simulations via finite element models, wherein each crystal of a polycrystal is resolved geometrically. Crystal plasticity

models have been implemented elsewhere to study shock loading of energetic materials cyclotetramethylene tetranitramine (HMX)¹⁰ and pentaerythritol tetranitrate (PETN).^{11,12} One aim of the present work is development and implementation of a crystal plasticity model for RDX, a particular model which, to the authors' knowledge, has not been published elsewhere.

The single crystal elastic-plastic model developed here extends a previous model¹³ for cubic crystals loaded to possibly high pressures. Here, the model is applied to crystals with orthorhombic symmetry characteristic of RDX. Anisotropic elastic constants and pressure-dependent compressibility are considered from experimental literature.^{14–16} Six slip systems (from four different families of systems) are implemented following analysis of indentation loading profiles and surface impressions.^{5,6} The model is applied to study indentation, with a spherical indenter of (001), (021), and (210) faces of single crystals of RDX.

This paper is organized as follows: Constitutive theory and material properties are described in Sec. II. Indentation simulations are reported in Sec. III. Conclusions follow in Sec. IV. Notation of continuum mechanics is used, e.g., bold-face type for vectors and tensors all referred to fixed Cartesian coordinates. Summation applies over repeated indices.

II. THEORY

A. Single crystal model

Let $\mathbf{x} = \boldsymbol{\chi}(\mathbf{X}, t)$ denote the motion of material points of the body. The deformation gradient is

$$\nabla \boldsymbol{\chi} = \mathbf{F} = \mathbf{F}^E \mathbf{F}^P, \quad (1)$$

where $\nabla(\cdot)$ denotes the material gradient (i.e., $F_{aA} = \nabla_A \chi_a = \partial \chi_a / \partial X_A$), \mathbf{F}^E denotes thermoelastic deformation of the

^{a)}Author to whom correspondence should be addressed. Electronic mail: john.d.clayton1.civ@mail.mil.

crystal lattice, and \mathbf{F}^P represents plastic deformation due to slip. The spatial velocity gradient is

$$\dot{\mathbf{F}}\mathbf{F}^{-1} = \dot{\mathbf{F}}^E\mathbf{F}^{E-1} + \mathbf{F}^E\mathbf{F}^P\mathbf{F}^{E-1}, \quad (2)$$

where the plastic velocity gradient associated with slip rates, $\dot{\gamma}^k$, reference slip directions, \mathbf{s}_0^k , and reference slip plane normals, \mathbf{m}_0^k , on slip systems, k , is

$$\mathbf{L}^P = \dot{\mathbf{F}}^P\mathbf{F}^{P-1} = \sum_k \dot{\gamma}^k \mathbf{s}_0^k \otimes \mathbf{m}_0^k. \quad (3)$$

Slip system geometry is pushed forward to the current configuration via $\mathbf{s}^k = \mathbf{F}^E\mathbf{s}_0^k$ and $\mathbf{m}^k = \mathbf{F}^{E-T}\mathbf{m}_0^k$, where $(\cdot)^T$ denotes the transpose. From orthonormality of slip directions and slip plane normals, plastic deformation is isochoric; thus, $J = \det \mathbf{F} = \det \mathbf{F}^E > 0$. By the polar decomposition theorem, let $\mathbf{F}^E = \mathbf{R}^E\mathbf{U}^E$. A logarithmic thermoelastic strain measure is defined as $\boldsymbol{\varepsilon} = \ln \mathbf{U}^E$ and is split into deviatoric and volumetric parts as

$$\boldsymbol{\varepsilon} = \boldsymbol{\varepsilon}' + (1/3)\bar{\varepsilon}\mathbf{1}, \quad \bar{\varepsilon} = \text{tr} \boldsymbol{\varepsilon} = \ln J, \quad (4)$$

where $\mathbf{1}$ is the second-order unit tensor, and the trace of a second-order tensor is $\text{tr}(\cdot)$. Let $\boldsymbol{\sigma}$ denote the usual Cauchy stress tensor; stress in an unrotated coordinate system is $\mathbf{S} = \mathbf{R}^{E-1}\boldsymbol{\sigma}\mathbf{R}^E$.

Only the isothermal case is considered, an appropriate assumption for applications of the model discussed in Sec. III. Let the unrotated stress be split into deviatoric and hydrostatic parts,

$$\mathbf{S} = \mathbf{S}' + \bar{S}\mathbf{1}, \quad \bar{S} = (1/3)\text{tr} \mathbf{S} = (1/3)\text{tr} \boldsymbol{\sigma} = -p, \quad (5)$$

with p the Cauchy pressure. The following operator extracts the deviatoric part of a second-order tensor,

$$\mathbb{I}' = \mathbb{I} - (1/3)\mathbf{1} \otimes \mathbf{1}, \quad \mathbb{I}'_{ABCD} = \delta_{AC}\delta_{BD} - (1/3)\delta_{AB}\delta_{CD}. \quad (6)$$

Constitutive equations for deviatoric stress and pressure are¹³

$$\mathbf{S}' = \mathbb{I}' : \mathbb{C} : \boldsymbol{\varepsilon}' + (1/3)(\mathbb{I}' : \mathbb{C} : \mathbf{1})\bar{\varepsilon}, \quad (7)$$

$$p = (B_0/B')[\exp(-B'\bar{\varepsilon}) - 1] - (1/3)\boldsymbol{\varepsilon}' : \mathbb{C} : \mathbf{1}. \quad (8)$$

Here, B_0 and B' are the reference bulk modulus and pressure derivative of the bulk modulus and \mathbb{C} is the tensor of second-order elastic constants referred to the (unrotated) crystal frame. The colon denotes contraction over two pairs of indices, e.g., $(\mathbb{C} : \boldsymbol{\varepsilon}')_{AB} = \mathbb{C}_{ABCD}\boldsymbol{\varepsilon}'_{CD}$. Pressure dependence of shear elastic coefficients, implemented elsewhere for cubic crystals,¹³ is omitted in Eq. (8) because of limited experimental data for the material of present interest.

The flow rule for slip is¹³

$$\boldsymbol{\tau}^k = \boldsymbol{\sigma} : (\mathbf{s}^k \otimes \mathbf{m}^k) = \tau_0^k [(|\dot{\gamma}^k| + \xi)/\dot{\gamma}_0]^m \text{sgn}(\dot{\gamma}^k). \quad (9)$$

The resolved shear stress on slip system k is τ^k . Material parameters are initial and constant slip strength, τ_0^k , for each slip system, reference strain rate, $\dot{\gamma}_0$, and rate sensitivity, m . Constant $\xi \ll \dot{\gamma}_0$ provides a finite strength at zero strain rate.

TABLE I. Structural and physical properties of RDX single crystals (ambient).

Property	Value	Ref.
Space group	<i>Pbca</i>	5
Crystal structure	Orthorhombic	
Lattice parameters [nm]	$a = 1.3182$	5
	$b = 1.1574$	
	$c = 1.0709$	
Mass density [g/cm ³]	1.806	16

B. RDX

Physical properties of RDX single crystals are listed in Table I. The description applies to the α phase, the stable polymorph for pressures under ≈ 3.8 GPa and temperatures under ≈ 480 K.

Elastic properties are listed in Table II. Isentropic second-order elastic constants^{15,16} and bulk modulus have been converted to isothermal values at 295 K via the usual thermodynamic formulae,¹⁷ incorporating anisotropic thermal expansion¹⁸ and specific heat.¹⁹ Voigt's notation is used: $\mathbb{C}_{ABCD} \leftrightarrow C_{\alpha\beta}$, where Greek indices 1, 2, ..., 6. Voigt (G_V) and Reuss (G_R) bounds¹⁷ on the effective shear modulus are also listed. Differences between Voigt and Reuss bounds for bulk modulus B_0 , on the order 1–3%, are considered insignificant.

As is evident from Table II, reported values of second-order elastic constants can vary substantially. Values obtained using resonant ultrasonic (RUS) methods¹⁵ listed in Table II are in reasonably close agreement with those reported by other researchers using the same method.²⁰ Values obtained using Brillouin scattering¹⁶ listed in Table II are notably different, with particularly larger bulk stiffness and shear stiffness in certain directions. Values obtained using a third technique, impulsive stimulated thermal scattering,²¹ are similar to those obtained using RUS. Possible reasons for differences among measurements of elastic constants of organic molecular crystals are discussed elsewhere.²² Values predicted using empirical atomic models^{23,24} also exhibit differences from those obtained in experiments, though these predicted values tend to align

TABLE II. Isothermal second-order elastic constants of RDX (converted from ambient isentropic values).

Property	Value ¹⁵	Value ¹⁶
C_{11} [GPa]	24.56	36.48
C_{22} [GPa]	18.85	24.49
C_{33} [GPa]	17.33	20.78
C_{12} [GPa]	7.61	0.90
C_{13} [GPa]	5.30	1.26
C_{23} [GPa]	5.24	8.16
C_{44} [GPa]	5.15	11.99
C_{55} [GPa]	4.06	2.72
C_{66} [GPa]	6.90	7.68
B_0 [GPa]	10.5	11.2
G_V [GPa]	6.06	9.26
G_R [GPa]	5.72	6.40

more closely with those from RUS than from Brillouin scattering.

In this work, the two sets of elastic constants^{15,16} are used, because these are the softest and stiffest reported experimental measurements, respectively; results obtained using these two sets might be expected to bound the actual response. Results obtained using these particular RUS constants¹⁵ are very close to those that would be obtained using similar values.^{20,21}

Pressure and temperature dependencies of second-order elastic coefficients have been calculated using molecular dynamics;²³ however, these predicted values have not been validated using experiments, and some discrepancies exist among calculated second-order elastic constants at room temperature and experimental values.¹⁶ For this reason, in the present study, the nonlinear elastic model only incorporates pressure dependence of the compressibility obtained experimentally¹⁴ and not that of all elastic coefficients, specifically, $B' = 6.95$.

Crystal plasticity theories incorporating higher-order elastic constants have also been developed^{12,25} and might offer an improved description of effects of volumetric and shear deformations on tangent elastic moduli; such an approach is not pursued here, because higher-order elastic constants (e.g., 20 independent third-order constants for an orthorhombic crystal¹⁷) are unknown for RDX. In a crystal plasticity model of PETN,¹² a tetragonal crystal, the Cauchy relations were used to estimate unknown third-order elastic constants.

Potential slip systems in RDX—as identified from hardness versus orientation profiles,⁵ indentation force versus depth data,^{6,7} and residual surface impressions from indentation⁶—are listed in Table III. Slip system geometry (Fig. 1) is referred to a Cartesian system with axes (X_1, X_2, X_3) parallel to lattice vectors ($\mathbf{a}, \mathbf{b}, \mathbf{c}$). Listed initial slip system strengths are upper bounds estimated from analysis of load excursion data using the analytical Hertzian solution for frictionless spherical indentation into a semi-infinite, linear elastic, isotropic material.⁶ Other systems may become active (and those listed may become inactive) for loading regimes involving very different pressures, temperatures, and/or strain rates; e.g., molecular dynamics simulations⁸ suggest that partial dislocation loops may glide on (001)[010] during shock loading at pressure in excess of ≈ 1 GPa.

Strengths for various families of systems are varied parametrically between physically reasonable bounds on the order of the theoretical strength,^{6,7} where $G = G_R = 6.4$

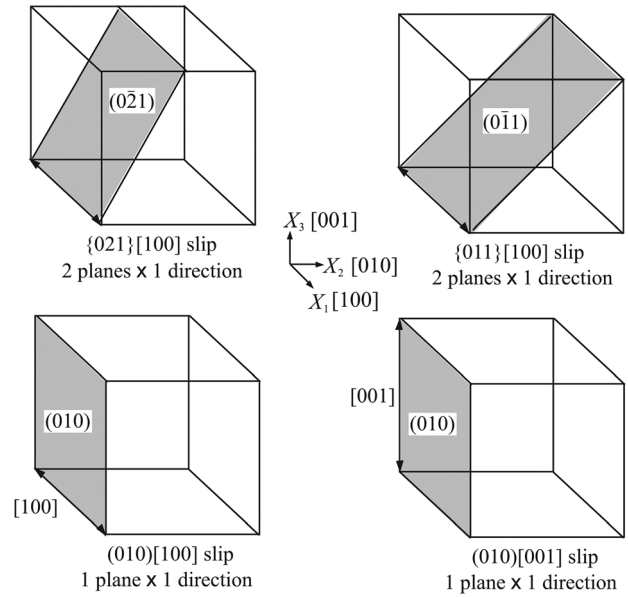


FIG. 1. Slip systems in RDX (unit cell parameters not to scale).

GPa.¹⁶ Because strengths of families of slip systems are not known precisely *a priori* from experiments, shear strengths, τ_0^k , are varied parametrically over the range listed in Table IV. This range is physically descriptive of homogeneous nucleation of glissile dislocation lines and loops.^{6,7,17} Other parameters, which provide a nearly rate-independent response, are also listed in Table IV.

III. INDENTATION

A. Boundary value problem

The constitutive model of Sec. II is implemented in the ALE3D multi-physics code. Simulations of indentation are performed using an implicit solver for static equilibrium.

The problem geometry mimics previous experimental studies.^{6,7} A spherical diamond indenter of radius $R = 1.482 \mu\text{m}$ is used to indent a flat surface of a single crystal of RDX of variable lattice orientation. Diamond is represented as an isotropic nonlinear elastic material with $B_0 = 443$ GPa, $G = 538$ GPa, and $B' = 4.0$.

The substrate is represented by a right circular cylinder.²⁶ The cylinder is assigned a height and radius of $2R$; further increases in dimensions of the cylinder did not affect results of interest. The indenter is modeled as a half-sphere. Each body is discretized using eight-node hexahedral elements with selective reduced integration. The mesh of the substrate is highly refined in the vicinity of contact beneath the indenter, where stress fields are inhomogeneous, and the

TABLE III. Slip systems in RDX single crystals (indentation).

System k	Miller indices	\mathbf{m}_0	\mathbf{s}_0	Max. strength [GPa]	Ref.
1	(021)[100]	(0, 0.880, 0.475)	[1, 0, 0]	0.885	5, 6
2	(0 $\bar{2}$ 1)[100]	(0, -0.880, 0.475)	[1, 0, 0]		
3	(011)[100]	(0, 0.679, 0.734)	[1, 0, 0]	0.645	5, 6
4	(0 $\bar{1}$ 1)[100]	(0, -0.679, 0.734)	[1, 0, 0]		
5	(010)[100]	(0, 1, 0)	[1, 0, 0]	0.885	6
6	(010)[001]	(0, 1, 0)	[0, 0, 1]	0.885	5, 6

TABLE IV. Crystal plasticity model parameters for RDX.

Property	Value
τ_0^k	$G/40 \leq \tau_0^k \leq G/10$
m	$\sim 5 \times 10^{-3}$
$\dot{\gamma}_0$	$10^{-2}/\text{s}$
ξ	$10^{-7}/\text{s}$

TABLE V. Elastic stiffness and Young's modulus of RDX oriented for indentation on planes (001), (021), and (210).

Stiffness	Plane [RUS ¹⁵]			Plane [Brillouin ¹⁶]		
	(001)	(021)	(210)	(001)	(021)	(210)
C_{11} [GPa]	24.56	24.56	20.15	36.48	36.48	22.17
C_{22} [GPa]	18.85	16.78	17.33	24.49	24.94	20.78
C_{33} [GPa]	17.33	17.62	23.06	20.78	26.98	28.29
E_{11} [GPa]	20.85	20.85	16.72	36.40	36.40	19.12
E_{22} [GPa]	15.69	14.05	15.40	21.28	22.84	18.04
E_{33} [GPa]	15.40	14.19	19.31	18.04	25.55	23.61

mesh coarsens progressively with distance from the initial contact point. Simulations with smaller elements demonstrated that further increases in mesh refinement did not affect results of interest.

During the loading phase, the upper face of the half-spherical indenter is assigned a constant (downward) velocity of $\dot{D} = 10$ nm/s in the laboratory X_3 -direction, leading to strain rates similar to those of experiments.⁶ The lower face of the cylinder is rigidly fixed, while the lateral sides (circumference) are traction-free. Indentation depth is denoted by D ; actual depth d of the tip of the sphere in contact with the surface is monitored as an outcome of the solution. Only for a rigid indenter would $d = D$. Indentation force P is the sum of nodal forces along the upper face of the half sphere acting in the direction of D , i.e., the sum of forces work conjugate to prescribed nodal velocities.

Contact between the indenter and substrate is assumed frictionless, following previous studies that rely on analytical solutions.^{6,7} Experimental measurements of dynamic friction for RDX single crystals sliding on a glass substrate²⁷ suggest

a friction coefficient on the order of unity for loads under 1 g (≈ 10 mN), wherein contact is characterized as elastic, and a friction coefficient of 0.35 for loads in excess of 10 g, wherein contact is characterized as plastic. The present indentation simulations consider a different geometry, smaller system sizes (loads under 1 g), and slower sliding velocities (on the order of 10 nm/s), so the reported experimental values for friction coefficients²⁷ may not strictly apply here. In additional simulations,²⁸ it was found that differences in indentation force among cases invoking frictionless and sticking contact were insignificant. In some simulations, unloading is also performed, whereby, after a peak depth is attained, the upper face of the indenter is assigned an upward velocity of $\dot{D} = 10$ nm/s until contact is released. If plastic deformation has occurred, then some residual deformation remains in the substrate upon unloading.

The present simulations enable direct quantification of surface and subsurface slip on each system. In contrast, hardness or indentation experiments⁵⁻⁷ require substantial interpretation of data to deduce slip activity and do not provide a quantitative measure of relative contributions of each slip system to the overall strain field. In the aforementioned experiments, visual observations of slip traces are restricted to residual surface profiles, whereas simulations enable visualization of subsurface slip activity.

Simulations of indentation onto (001), (021), and (210) planes are reported in Sec. III B. Let $\mathbb{C}^{(ijk)}$ be the fourth-order matrix of elastic constants of the crystal oriented for indentation into crystallographic plane (ijk) . Let $\mathbf{R}^{(ijk)}$ be the corresponding rotation matrix. Then,

$$\mathbb{C}_{ABCD}^{(ijk)} = R_{AE}^{(ijk)} R_{BF}^{(ijk)} R_{CG}^{(ijk)} R_{DH}^{(ijk)} \mathbb{C}_{EFGH}, \quad (10)$$

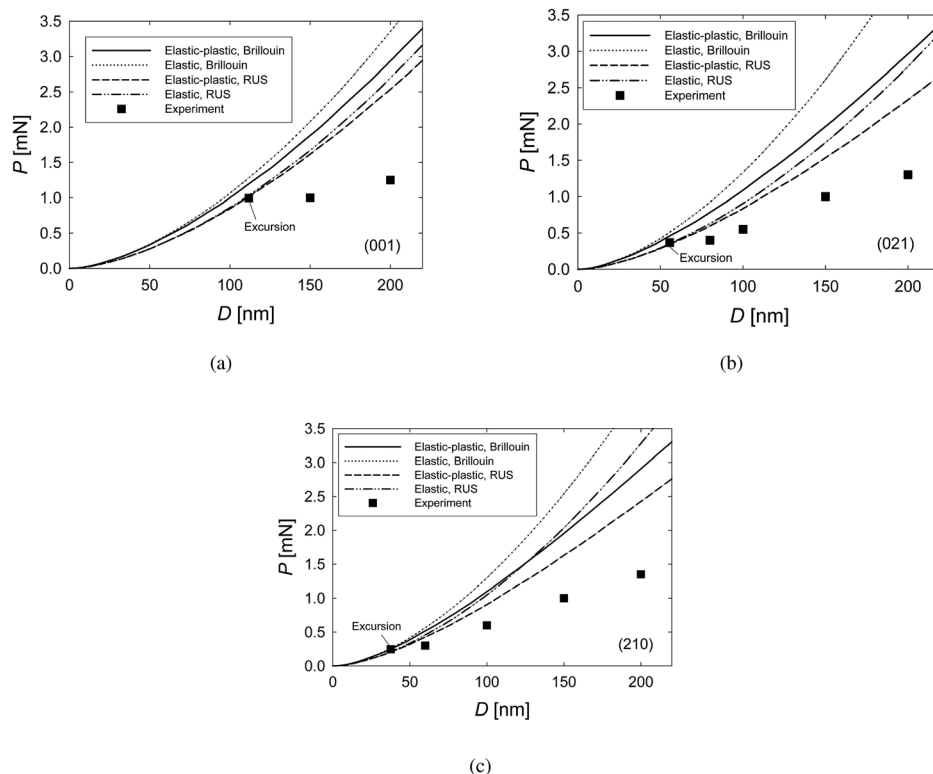


FIG. 2. Indentation force vs applied displacement; model predictions obtained using RUS (Ref. 15) and Brillouin (Ref. 16) elastic constants compared to experiment (Ref. 6): (a) indentation into (001); (b) indentation into (021); (c) indentation into (210).

where \mathbb{C}_{EFGH} corresponds to elastic constants of Table II. Values of elastic stiffness are listed in Table V. Perhaps most pertinent to indentation in the X_3 -direction, $C_{33}^{(210)} > C_{33}^{(021)} > C_{33}^{(001)}$ for either set of constants. Note that $C_{33}^{(ijk)}$ from Brillouin scattering¹⁶ always exceeds the corresponding value from RUS.¹⁵ Components of compliance $S_{\alpha\beta}$ are those of the inverse of $C_{\alpha\beta}$. Young's moduli are $E_{11} = 1/S_{11}$, $E_{22} = 1/S_{22}$, and $E_{33} = 1/S_{33}$. From Table V, $E_{\alpha\alpha}^{(ijk)}$ from Brillouin scattering¹⁶ always exceeds the corresponding value from RUS¹⁵ for $\alpha = 1, 2$, and 3.

B. Model predictions

Predictions obtained using each set of elastic constants^{15,16} are compared directly for substrate orientations (001), (021), and (210) in Fig. 2. In results marked as “elastic”, slip is suppressed to permit assessment of the elasticity model in isolation and to permit deduction of the yield point upon comparison with “elastic-plastic” results, wherein the slip model of Sec. II is enabled. For the latter results shown in Fig. 2, for each set of elastic constants, strength is set to a constant value of $\tau_0^k = G/20$ for all six slip systems.

Significantly closer agreement between model and experiment⁶ is obtained from the elastic constants from RUS¹⁵ for indentation onto (001) and (021) planes. The first experimental data point in each figure corresponds to the maximum depth at which the indentation process remains elastically reversible, i.e., initiation of the first excursion from a smooth force-displacement profile.^{6,7} Comparable accuracy is obtained from either set of elastic constants for indentation on (210) planes. The present simulations strongly suggest that elastic constants obtained from RUS^{15,20} provide a more realistic representation of elastic stiffness during nano-indentation than elastic constants obtained from Brillouin scattering,¹⁶ with the latter appearing too stiff. Results shown in Fig. 2 invoke the geometrically nonlinear elastic model with pressure-dependent bulk modulus; comparison with results of additional calculations²⁸ with $B' = 0$ for RDX demonstrated that the effect of nonlinear compressibility becomes noticeable for $D \gtrsim 50$ nm.

In simulations, the yield point (initiation of slip) can be deduced as the indentation depth beyond which elastic and elastic-plastic model predictions begin to differ. From Fig. 2, the predicted yield point matches the experimental excursion point reasonably well for each orientation when RUS elastic constants¹⁵ are used in the model. In contrast, the indentation depth at which yielding is predicted is premature for (001) and (021) orientations when Brillouin constants¹⁶ are used. This difference is presumably a result of attainment of larger resolved shear stresses at a given depth of indentation when stiffer constants are used.

Predicted forces exceed experimental values at larger indentation depths in each orientation and for both sets of elastic constants. Results corresponding to more compliant elastic constants¹⁵ provide closer agreement to experimental values than results corresponding to stiffer elastic constants.¹⁶ As noted elsewhere,^{26,28} uncertainty in the true tip radius, R , of the indenter could lead to discrepancies between

simulations and experiments. Surface fractures and/or sub-surface fractures could contribute to a loss of stiffness that would be reflected only in the experimental data. RDX is prone to cleavage fracture on planes (001), (010), (001), (241), and ($\bar{2}41$).^{2,4,6} Experimental data demonstrate nearly horizontal steps in force versus displacement corresponding to discrete shear discontinuities and/or fracture events that are not readily resolved by a constant strength continuum crystal plasticity model, such as the one formulated here. In

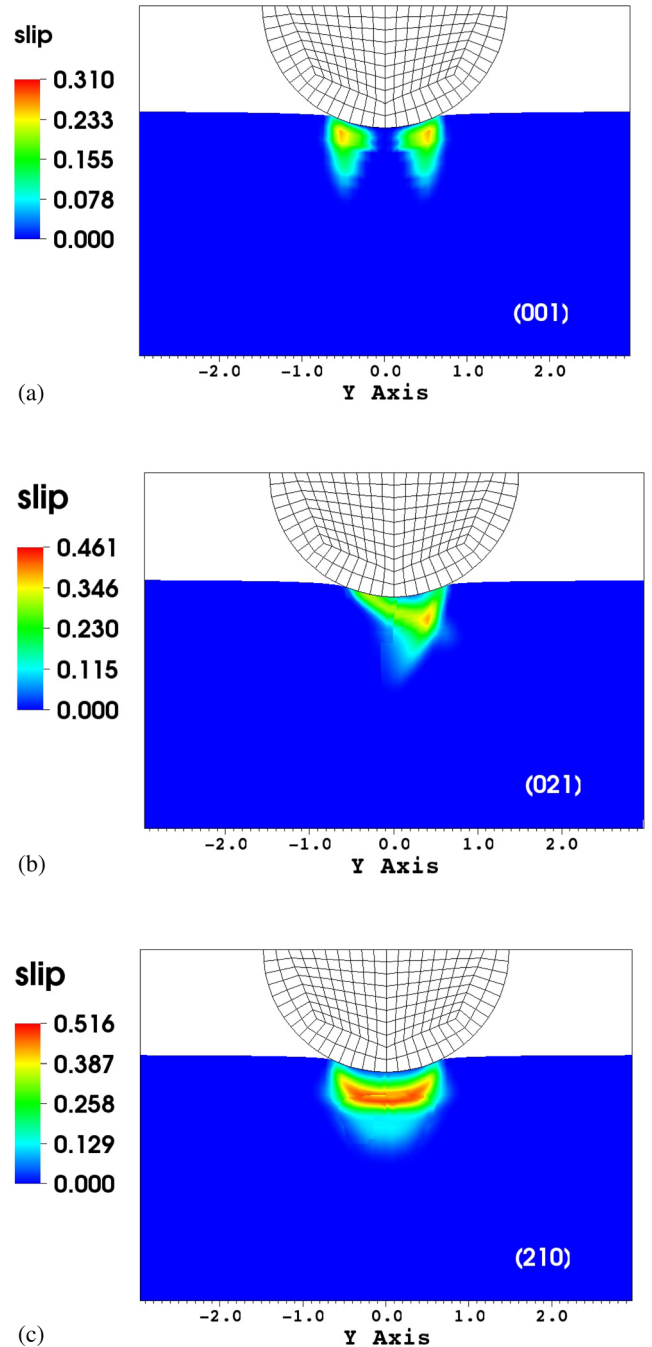


FIG. 3. Cumulative total slip contours for indentation to depth $D = 200$ nm using elastic constants from RUS (Ref. 15) and slip system strength $G/20$; a slice along the centerline of the cylinder normal to the laboratory X_1 axis is shown: (a) indentation into (001)[X-axis normal to (100)]; (b) indentation into (021)[X-axis normal to (100)]; (c) indentation into (210)[X-axis normal to ($\bar{2}30$)].

TABLE VI. Maximum local slip γ^k at indentation depth of 200 nm for indentation on (001), (021), and (210) planes; RUS elastic constants.¹⁵

System k	Plane (001)	Plane (021)	Plane (210)
1	0.01	0.19	0.40
2	0.01	0.00	0.40
3	0.08	0.16	0.29
4	0.08	0.00	0.29
5	0.00	0.10	0.51
6	0.31	0.41	0.16
all (γ)	0.31	0.46	0.52

TABLE VII. Maximum local slip γ^k at indentation depth of 200 nm for indentation on (001), (021), and (210) planes; Brillouin elastic constants.¹⁶

System k	Plane (001)	Plane (021)	Plane (210)
1	0.01	0.19	0.41
2	0.01	0.00	0.41
3	0.06	0.13	0.28
4	0.06	0.00	0.28
5	0.01	0.10	0.52
6	0.35	0.51	0.26
all (γ)	0.35	0.56	0.58

experiments,⁶ surface fractures are detected only at loads significantly exceeding yield excursion.

Details of slip system interactions and pressure dependence of shear strength are omitted in the present model. Indentation experiments have suggested the importance of cross slip,⁶ and atomic modeling has noted that different slip mechanisms may become important at high pressures.⁸ Incorporation of these effects into a more complex slip model might provide closer agreement with experiment, e.g., if glide resistance were to decrease with pressure, since local pressures under the indenter can achieve several GPa.²⁸ Atomic modeling^{8,24} may provide insight into dependence of slip resistance on pressure (and temperature, etc.) not available from experimental methods.

Model predictions of cumulative slip for indentation to a depth of $D = 200$ nm onto planes (001), (021), and (210) are shown in Fig. 3. In each case, a slice along the centerline of the cylinder normal to the laboratory X_1 axis (i.e., X -axis) is shown. For indentation on (001) and (021) planes, the X_1 axis is normal to a (100) plane; for indentation on (210), the X_1 axis is approximately normal to a (2 $\bar{3}$ 0) plane. Cumulative total slip, γ , is defined as

$$\gamma = \sum_k \gamma^k = \sum_k \int |\dot{\gamma}^k| dt, \quad (11)$$

with γ^k the monotonically increasing cumulative slip on system k . Slip activity is greater for indentation into (021) and (210) planes than for indentation on (001). For this particular viewing plane, slip contours for indentation on (021) are noticeably asymmetric. The wireframe mesh of the indenter is drawn in each figure; in order to enable clear visualization of heterogeneous slip distributions in the RDX, the mesh of

the substrate, which is considerably more refined than that of the indenter, is not shown.

Tables VI and VII list maximum local cumulative slip (i.e., the maximum value of γ^k at any location in the RDX substrate) at an indentation depth $D = 200$ nm when various elastic constants^{15,16} are implemented. Total slip, γ , listed in the bottom row of each table is not necessarily the sum of all γ^k listed in a given column, because the location in the substrate where total slip is maximum does not necessarily correspond to the location where each γ^k is maximum. Orientation (001) exhibits slip primarily on system 6. Significant activity of multiple slip systems is evident for indentation onto (021) and (210) planes. Trends are qualitatively similar, regardless of choice of elastic constants. Cumulative slip magnitudes are generally slightly larger in Table VII than in Table VI, because larger stresses are attained at the same depth of indentation when stiffer elastic constants are prescribed.

Elastic-plastic simulations were also performed, wherein the strength, τ_0^k , of one family of systems was set to $G/20$, with that of all others set to $G/10$. Comparison of force versus depth profiles among these simulations enabled further assessment of the most active slip systems for each crystal orientation.²⁸ Results were consistent with those in Tables VI and VII: slip system 6 is dominant for indentation on (001) and (021), while systems 1–5 are all important for indentation on (210).

Model predictions for uniform slip strengths, τ_0^k , of $G/10$, $G/20$, and $G/40$ are compared with experimental data⁶ in Fig. 4 for indentation on (210). Reduction of slip strength from $G/20$ to $G/40$ enables closer agreement with experiment at larger indentation depths, but also leads to premature initiation of slip and under-prediction of force at smaller depths

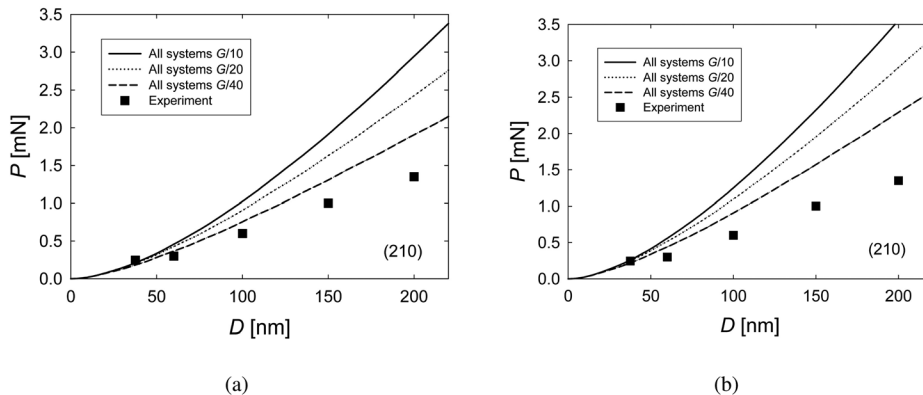


FIG. 4. Indentation force vs applied displacement for elastic-plastic indentation into plane (210) with uniform slip strengths $G/10$, $G/20$, and $G/40$ compared to experiment (Ref. 6); model predictions obtained using (a) RUS (Ref. 15) and (b) Brillouin (Ref. 16) elastic constants.

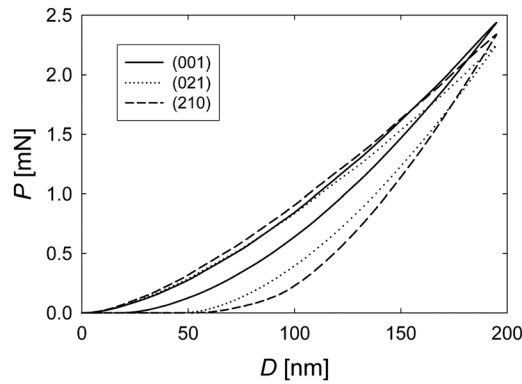


FIG. 5. Indentation force vs applied displacement for a single load-unload cycle on each of (001), (021), and (210) planes; elastic constants from RUS (Ref. 15), uniform slip strength $G/20$.

near experimental excursion points, i.e., near initial yield. Similar trends were predicted²⁸ for indentation onto (001) and (021) planes when strength is increased or decreased uniformly among slip systems.

Loading-unloading simulations of indentation on (001), (021), and (210) planes were performed to enable comparison with experimental observations. Force versus displacement predictions are shown in Fig. 5 for a single load-unload cycle, corresponding to loading to $D \approx 200$ nm and then unloading to $D=0$. During much of the loading phase, orientation (001) is slightly less stiff than orientations (021) and (210). However, at $D \approx 200$ nm, P is largest for orientation (001). Recall that orientation (001) demonstrates a lower elastic stiffness, but also less slip

activity. Hence, at larger indentation depths, increased slip activity for orientations (021) and (210) lowers their effective tangent stiffness and, hence, P below that of orientation (001). Hysteresis is also substantially greater for indentation on (021) and (210) than for (001), again demonstrating less slip activity in the latter. Orientation (210) demonstrates the most hysteresis (and greatest slip activity) and the largest elastic stiffness for much of the unloading phase.

Figure 6 shows total cumulative slip, γ , on unloaded surfaces of (001), (021), and (210) planes. In each case, the maximum indentation depth prior to unloading is $D \approx 200$ nm. Non-circular contours are consistent with activity of fewer than five geometrically independent systems necessary to accommodate an arbitrary plastic strain field.⁶

Surface slip contours from individual systems were also examined.²⁸ Predicted surface slip activity results primarily from system 6 for indentation on (001). Slight contributions to the circular total slip trace in Fig. 6(a) are due to systems 3 and 4, i.e., $\{011\}[100]$. Surface slip activity is predominantly from system 6, with minor contributions from systems 1 and 3, for indentation on (021). Surface slip activity is predominantly from system 5, with contributions from systems 1, 2, and 6, for indentation on (210). Faint contributions from systems 3 and 4 are also predicted for indentation on (210).

Active slip planes during the loading history at the specimen surface, as predicted here, are compared with those deduced from experimental surface impressions⁶ in Table VIII. It is noted that, in simulations of indentation on (210),

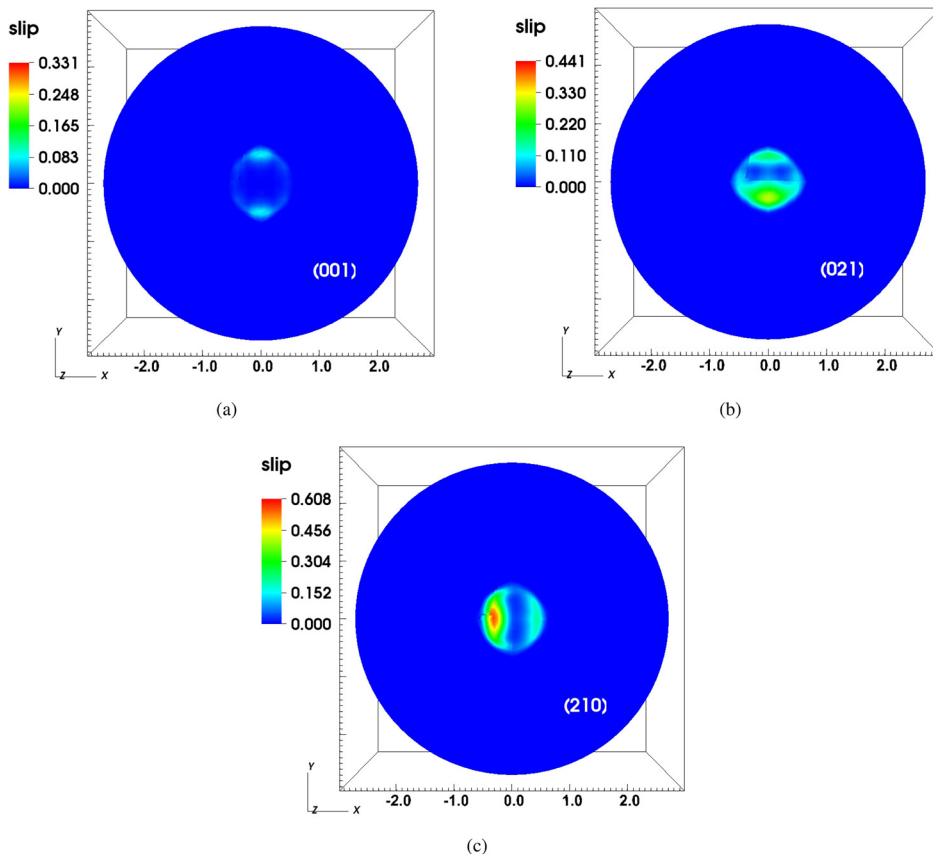


FIG. 6. Residual total slip contours at the surface for indentation to depth $D \approx 200$ nm followed by unloading; results obtained using elastic constants from RUS (Ref. 15) and uniform slip system strength $G/20$: (a) indentation into (001); (b) indentation into (021); (c) indentation into (210).

TABLE VIII. Significantly active slip planes at the specimen surface during indentation of (001), (021), and (210) planes.

Indentation surface	Present results	Experiment ⁶
(001)	(010), {011}	(010), {011}, {021}
(021)	(010), (011), (021)	Not reported
(210)	(010), {011}, {021}	(010), {011}, {021}

systems 3 and 4, i.e., {011}[100], demonstrate substantial activity within the bulk material (i.e., beneath the surface), but little cumulative slip at the surface. Though not presented graphically in this paper, predicted residual bulk and surface slip contours were also obtained using the relatively stiff elastic constants from Brillouin scattering.¹⁶ Predicted slip contours appeared qualitatively similar, regardless of choice of elastic constants from RUS¹⁵ or Brillouin.¹⁶

IV. CONCLUSIONS

A nonlinear anisotropic elastic-plastic model has been developed for RDX. The model accounts for orthorhombic elastic constants, pressure-dependent compressibility, and dislocation glide on up to six distinct slip systems.

Numerical simulations of spherical indentation on (001), (021), and (210) planes of single crystals show significant influences of elastic anisotropy and nonlinearity on force-displacement data. Model predictions for initial elastic response using constants measured with resonant ultrasound spectroscopy agree with experimental force-displacement data for indentation on (001), (021), and (210) planes. Predictions using constants measured with Brillouin scattering are in reasonable agreement with experiments for indentation on (210), but are stiffer than experiments for indentation on (001) and (021). Orientation (001) is elastically most compliant, in agreement with experiments.

Critical shear strengths associated with slip initiation have been estimated as $G/20$, where G is a representative elastic shear modulus. Initial yield points predicted by the model are in close agreement with experimental load excursion data when elastic constants from resonant ultrasound spectroscopy are used. Predictions of force for larger indentation depths, wherein predicted plastic slip is substantial, tend to exceed experimental values, regardless of which set of elastic constants is used. The constant strength (i.e., perfectly plastic) slip model implemented here is unable to replicate nearly horizontal steps in indentation force observed in experiments. Such steps may correspond to discrete slip events of width too fine to be captured by a conventional continuum slip model. Dependencies of shear strength on slip history and pressure have been omitted; incorporation of such physics, for example, as suggested by atomic simulations, might provide improved agreement. Fractures observed in experiments (at the surface) or not observed (subsurface) would also explain the higher stiffness in simulations relative to experiments.

Simulations suggest that slip planes (010) and {011} contain active systems for indentation on (001), with slip on

system (010)[001] dominating the inelastic response; experimental surface observations confirm that these, as well as {021} slip planes, may also be active. Simulations suggest that slip planes (010) and {021}, and to a lesser extent {011}, are active at the specimen surface for indentation on (210); these same planes have also been confirmed as active in experiments. Simulations suggest that planes (010), (011), and (021) contain active systems for indentation on (021); particular slip planes active for this orientation have not been reported from experiments.

The present results suggest that system (010)[001] provides the largest contribution to the inelastic material response (i.e., post-yield force versus displacement curve) for indentation on (001) and (021) planes, while five systems {021}[100], {011}[100], and (010)[100] all contribute to inelastic response for indentation on (210) planes. Plastic deformation and hysteresis are more extensive for indentation on (021) and (210) than for indentation on (001). Since much plastic deformation occurs in the bulk of the material, and since different slip mechanisms may be prominent at the surface and in the bulk, the present results offer new insight into inelastic mechanical behavior of RDX not available from experimental observations of residual surface topography alone.

The model developed here, when used with elastic constants obtained from resonant ultrasonic methods, is thought to provide an accurate representation of the nonlinear anisotropic response of RDX single crystals up to and including the onset of slip. The present model is also thought to provide a qualitatively reasonable depiction of activity of different slip systems when a uniform and constant shear strength on the order of $G/20$ is prescribed. Refinements of the model are needed to address any reduction in stiffness associated with discrete or highly localized shear events or cleavage fractures observed at larger indentation depths.

¹D. E. Hooks, K. J. Ramos, and A. R. Martinez, *J. Appl. Phys.* **100**, 024908 (2006).

²W. Connick and F. G. J. May, *J. Cryst. Growth* **5**, 65 (1969).

³P. J. Halfpenny, K. J. Roberts, and J. N. Sherwood, *J. Cryst. Growth* **65**, 524 (1983).

⁴W. L. Elban, R. W. Armstrong, K. C. Yoo, R. G. Rosemeier, and R. Y. Yee, *J. Mater. Sci.* **24**, 1273 (1989).

⁵H. G. Gallagher, P. J. Halfpenny, J. C. Miller, and J. N. Sherwood, *Philos. Trans. R. Soc. London, Ser. A* **339**, 293 (1992).

⁶K. J. Ramos, D. E. Hooks, and D. F. Bahr, *Philos. Mag.* **89**, 2381 (2009).

⁷K. J. Ramos, D. F. Bahr, and D. E. Hooks, *Philos. Mag.* **91**, 1276 (2011).

⁸M. J. Cawkwell, K. J. Ramos, D. E. Hooks, and T. D. Sewell, *J. Appl. Phys.* **107**, 063512 (2010).

⁹K. J. Ramos, D. E. Hooks, T. D. Sewell, and M. J. Cawkwell, *J. Appl. Phys.* **108**, 066105 (2010).

¹⁰N. R. Barton, N. W. Winter, and J. E. Reaugh, *Modell. Simul. Mater. Sci. Eng.* **17**, 035003 (2009).

¹¹J. J. Rimoli, E. Gurses, and M. Ortiz, *Phys. Rev. B* **81**, 014112 (2010).

¹²J. M. Winey and Y. M. Gupta, *J. Appl. Phys.* **107**, 103505 (2010).

¹³R. Becker, *Int. J. Plast.* **20**, 1983 (2004).

¹⁴B. Olinger, B. Roof, and H. H. Cady, *Proceedings of the International Symposium on High Dynamic Pressures* (Commissariat à l'Energie Atomique, Paris, 1978), pp. 3–8.

¹⁵S. Haussuhl, *Z. Kristallogr.* **216**, 339 (2001).

¹⁶J. J. Haycraft, L. L. Stevens, and C. J. Eckhardt, *J. Chem. Phys.* **124**, 024712 (2006).

¹⁷J. D. Clayton, *Nonlinear Mechanics of Crystals* (Springer, Dordrecht, 2011).

- ¹⁸H. H. Cady, *J. Chem. Eng. Data* **17**, 369 (1972).
- ¹⁹D. Bedrov, J. B. Hooper, G. D. Smith, and T. D. Sewell, *J. Chem. Phys.* **131**, 034712 (2009).
- ²⁰R. B. Schwarz, D. E. Hooks, J. J. Dick, J. I. Archuleta, and A. R. Martinez, *J. Appl. Phys.* **98**, 056106 (2005).
- ²¹B. Sun, J. M. Winey, N. Hemmi, Z. A. Dreger, K. A. Zimmerman, Y. M. Gupta, D. H. Torchinsky, and K. A. Nelson, *J. Appl. Phys.* **104**, 073517 (2008).
- ²²L. L. Stevens, D. E. Hooks, and A. Migliori, *J. Appl. Phys.* **108**, 053512 (2010).
- ²³T. D. Sewell and C. M. Bennett, *J. Appl. Phys.* **88**, 88 (2000).
- ²⁴L. B. Munday, P. W. Chung, B. M. Rice, and S. D. Solares, *J. Phys. Chem. B* **115**, 4378 (2011).
- ²⁵J. D. Clayton, *Proc. R. Soc. Ser. A* **465**, 307 (2009).
- ²⁶R. Nowak, T. Manninen, K. Heiskanen, T. Sekino, A. Hikasa, K. Niihara, and T. Takagi, *Appl. Phys. Lett.* **83**, 5214 (2003).
- ²⁷J. K. A. Amuzu, B. J. Briscoe, and M. M. Chaudhri, *J. Phys. D: Appl. Phys.* **9**, 133 (1976).
- ²⁸J. D. Clayton and R. C. Becker, U.S. Army Res. Lab. Tech. Report ARL-TR-5864, 2012.

NO. OF
COPIES ORGANIZATION

1 DEFENSE TECHNICAL
(PDF INFORMATION CTR
only) DTIC OCA
8725 JOHN J KINGMAN RD
STE 0944
FORT BELVOIR VA 22060-6218

1 DIRECTOR
US ARMY RESEARCH LAB
IMNE ALC HRR
2800 POWDER MILL RD
ADELPHI MD 20783-1197

1 DIRECTOR
US ARMY RESEARCH LAB
RDRL CIO LL
2800 POWDER MILL RD
ADELPHI MD 20783-1197

1 DIRECTOR
US ARMY RESEARCH LAB
RDRL D
2800 POWDER MILL RD
ADELPHI MD 20783-1197

NO. OF
COPIES ORGANIZATION

ABERDEEN PROVING GROUND

49 DIR USARL
RDRL CIH C
P CHUNG
J KNAP
L MUNDAY
RDRL WM
B FORCH
J MCCAULEY
RDRL WML
J NEWILL
RDRL WML B
I BATYREV
J BRENNAN
E BYRD
S IZVYEKOV
J MOORE
R PESCE-RODRIGUEZ
B RICE
D TAYLOR
N WEINGARTEN
RDRL WML H
B SCHUSTER
RDRL WMM B
G GAZONAS
D HOPKINS
RDRL WMP
S SCHOENFELD
RDRL WMP B
C HOPPEL
R KRAFT
D POWELL
S SATAPATHY
M SCHEIDLER
T WEERASOORIYA
RDRL WMP C
R BECKER
S BILYK
T BJERKE
D CASEM
J CLAYTON (10 CPS)
D DANDEKAR
M GREENFIELD
B LEAVY
M RAFTENBERG
S SEGLETES
C WILLIAMS
RDRL WMP F
N GNIAZDOWSKI
RDRL WMP G
R EHLERS
N ELDREDGE
S KUKUCK

INTENTIONALLY LEFT BLANK.